Solution-processed Synthesis-in-Place Method of Hematite Nanorods for Selective Ethanol and Acetone Sensors

산화철 나노로드 표적지점 용액기반 합성법을 이용한
에탄올-아세톤 고선택성 가스센서

2017년 8월

서울대학교 대학원

재료공학부

이선용

Abstract

Solution-processed Synthesis-in-Place Method of Hematite Nanorods for Selective Ethanol and Acetone Sensors

Seonyong Lee

Department of Materials Science and Engineering

College of Engineering

Seoul National University

Integrating highly crystalline hematite nanorods with patterned substrates is an effective design strategy for taking advantage of one-dimensional nanorod structures such as high surface-to-volume ratio and long-term reliability, but many challenges remain in synthesis. Here we report a facile synthesis-in-place method for hematite nanorod films on patterned substrates without additional process and

the application of the films to gas sensors. Vertically standing hematite nanorods are synthesized with hydrothermal method. The morphology of hematite nanorods is controlled by changing synthesis time. It is shown that the response of vertically standing hematite nanorods to 50 ppm ethanol at 350°C is 4 times higher than that of collapsed nanorods and the theoretical detection limit is estimated to be about 20 ppb. This is explained with gas accessibility to the bottom region of the oxide layer, so called, utility factor. The nanorod sensor shows selective responses to ethanol at 300-375 $^{\circ}$C and to acetone at 400°C. Our results demonstrate that the morphology control using the facile synthesizing method is an effective strategy for making ethanol or acetone sensors based on the earth-abundant semiconducting oxide, hematite.

Contents

Abstract

Contents

List of tables

List of figures

List of tables

List of figures

Figure 2.1 Schematic diagram for change of the sensor resistance upon exposure to reducing gas (target gas) in the cases of n-type and p-type semiconductor sensors

Figure 2.2 Conduction mechanisms in metal oxide gas sensitive materials according to the grain size. (a) D < 2L, grain boundary control; (b) D = 2L, neck control; (c) D > 2L, grain control.

Figure 4.1 Photographs of a fabricated SiO_2/Si substrate (a) before annealing, (b) after annealing, and photographs of bare SiO_2/Si substrate synthesized (c) with ketone tape, (d) without tape.

Figure 4.2 (a) Optical microscope image of hematite nanorods array on Pt IDE patterned SiO2/Si substrate. (b) High-magnification SEM image of selected area in (a). (c) cross-sectional SEM image of hematite nanorods array.

Figure 4.3 (a-d) Plain-view SEM image of (a) S1, (b) S2, (c) S3, (d) S4 and (e-h) cross-sectional SEM image of (e) S1, (f) S2, (g) S3, (h) S4

Figure 4.4 (a) Low-magnification TEM image of scraped hematite nanorod. (b) High-magnification TEM image of hematite nanorod. The inset shows selected area diffraction pattern with indexing.

Figure 4.5 Glancing angle X-ray diffraction patterns of hematite nanorods array S1~S4.

Figure 4.6 Response curves of S1, S2, S3, S4 to 50ppm (a) acetone, (b) ethanol, and (c) toluene. Red, blue, green and gray curves are response of S1, S2, S3, and S4, respectively.

Figure 4.7 (a) Response of S2 to 50ppm acetone, ethanol and toluene as a function of temperature. (b) Response of S1~S4 at 350oC to 50 ppm acetone, ethanol, and toluene.

Figure 4.8 (a) Sensing transient of S2 to various gases. (b) Response of S2 to various gases.

Figure 4.9 (a) Theoretical detection limits (DL) of S2 to ethanol. Inset shows response curve to 10-50 ppm ethanol at 350ºC. (b) Response to 9 consecutive pulse of S2 to 10-50 ppm ethanol.

Figure 4.10 Schematic drawing of hematite nanostructure (a) with complete rods (b) with porous rods. Molecules at top side are sphere model of ethanol and yellow sphere is electron. Green line is gas acceptance way and yellow line is current path.

Chapter 1.

Introduction

Gas sensors, monitoring real-time change of gaseous chemical analytes, based on semiconducting materials are essential for environmental monitoring, industrial safety, medical diagnosis and automobile fuel combustion control[1-3]. Recently, as internet of things (IoT), interconnected devices able to exchange data about the nearby environment with users and other devices, attracts interests, monitoring air quality becomes integral function to the every electronics. Hematite, the most abundant metal oxide n-type semiconductor in the earth, has been known as one of the great candidates as a gas sensing material, owing to moderate band gap (2.2eV) and high chemical stability[4-6]. However, gas sensors based on hematite do not have much attention due to their low sensitivity and slow response compared with gas sensors based on metal oxide like SnO_2[7-10]. To overcome these problems and to improve the gas sensing properties, many studies have focused on synthesizing hematite nanostructures due to their large surface areas and increased surface activity and enhanced adsorption of the target gas molecules.

Recently, 0-dimensional (0D) nanomaterials like nanoparticles and hollow nanoparticles have been used for active materials in conventional gas sensors. However, 0D nanomaterials are easily aggregated each other, so gas molecules are hardly diffused into nanostructures. Alternatively, 1-dimensional (1D) nanomaterials such as nanotubes, nanowires, nanobelts and nanorods have been studied since gas molecules are easily diffused into the interstitial space between nanostructures and absorbed onto the surface of 1D nanomaterials from

top to bottom. However, a few problems still remain unsolved, such as production in large scale and low cost process of synthesizing one-dimensional hematite nanostructures.

Of the two main approaches to synthesize gas sensors based on 1D hematite nanostructures, the first is the electrochemical anodization of titanium[11-13]. Resultant TiO_2 nanotube arrays on Ti substrates can act as chemical sensing layers with high sensitivity to formaldehyde, acetone, and ethanol at room temperature. In addition, high sensitivity to H_2 has been reported from Pd-doped TiO_2 nanotubes arrays. Nonetheless, such nanotube arrays have not been exploited for chemiresistors operating at elevates temperatures for the detection of a wide variety of chemical vapors because the conducting Ti substrates easily form electrical shorts with the sensor electrodes. In addition, the Ti substrates are not compatible with high throughput semiconductor fabrication processes.

The second approach is the use of the hydrothermal method to synthesize hematite nanostructures. Hydrothermal method is solution-based method which does not need vacuum condition. Simple process and high crystalline is the most popular advantage of this method. However, in gas sensing area, it is difficult to synthesize on foreign substrate, usually drop-casting after homogeneous nucleation is used[14, 15]. Heterogeneous nucleation on each substrate is important goal for low-cost and high-yield mass production.

No work has been reported on direct synthesis of hematite gas sensors

due to tough nucleation on typical SiO_2 substrate. The key idea of our hydrothermal method to achieve directly grown hematite nanomaterials is the use of Pt interdigitated electrodes (IDEs) on SiO_2/Si substrate. Pt bottom electrodes help hematite thin films based on 1D nanomaterials uniformly grown on SiO_2 between Pt finger electrodes since hematite is easily grown on metal substrate such as Pt and Fe. This strategy has not been applied to the synthesis of hematite thin films based on 1D nanomaterials.

Here, we report the comparative acetone, ethanol and toluene sensing behaviors of directly synthesized hematite nanorods using hydrothermal method for sensor applications. The sensors prepared by hydrothermal methods on Pt IDEs present successful distinct between acetone and ethanol by different optimized operating temperature. The responses to various gases such as CO, C_6H_6, NH_3, H_2, and CH_3CHO also have been measured at 350^oC. In addition, gas diffusion into interstitial space of 1D nanomaterials enhances the interaction between target gases and sensing materials, resulting in theoretical detection limit to ethanol at a parts-per-billion (ppb) level.

Chapter 2.

Literature survey

2.1 Working principle

Semiconductor gas sensors, typically based on metal-oxide semiconductor, work on a simple mechanism, detecting the change of their electrical conductivity. In general, the chemisorption of oxygen is considered as main factor in the change of electrical properties of the sensors. Molecular oxygen absorbed on the surface of the sensors by attracting and trapping electrons from the conduction band of the semiconductor as shown in the Eq. 2.1.

$$O_2(gas) + e^- \Leftrightarrow O_2^-(absorb) \tag{2.1}$$
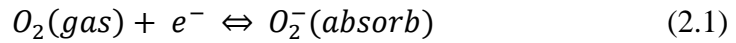
According to operating temperature of each sensors, the oxygen ion molecules are dissociated into oxygen ion atoms by thermal energy and electrons from the conduction band.

$$\frac{1}{2}O_2 + e^- \Leftrightarrow O_{ads}^- \tag{2.2}$$

$$\frac{1}{2}O_2 + 2e^- \Leftrightarrow O_{ads}^{2-} \tag{2.3}$$

Semiconductor gas sensors based on metal oxides can be classified into two groups, n-type such as SnO_2, ZnO, WO_3, TiO_2, Fe_2O_3 and p-type such as NiO, Co_3O_4, CuO according to the major carriers. Also, target gas species can be

divided into two groups, oxidizing gas (electron acceptors) and reducing gas (electron donor). The change of gas sensor resistance depends on a type of sensing materials and target gas.

n-type semiconductor gas sensor

For n-type semiconductors, space-charge layer, namely, electron depletion regions are formed on the surface of oxide material when the oxygen molecules absorbed on the surface. In contrast, upon to exposure to reducing gases, including CH_3COCH_3, C_7H_8, H_2, CO, C_2H_5OH, NH_3, H_2S and CH_4, the adsorbed oxygen molecules on the surface of n-type semiconductor reacts with these gases to release trapped electrons, which can reverse the band bending with decrease of electrical resistance. When the n-type semiconductors are exposed to oxidizing gases such as O_2, CO_2, Cl_2, NO and NO_2, these gases directly adsorb on the surface of oxide material to form negatively charged ions, resulting that the electric resistance is conversely increased by the expansion of electron depletion regions.

p-type semiconductor gas sensor

For p-type semiconductor, they show an opposite behavior compared with n-type semiconductor gas sensors. Upon exposure to reducing gases, the

resistance of the p-type semiconductor is increased due to recombination between generated holes and released electrons. On the other hand, when the p-type semiconductor is exposed to oxidizing gases, gas molecules also adsorb on oxide surface and attract surface electrons to form negative charged ions, resulting in the decrease of the resistance. A summary of response is shown in Tab. 2.1 and Fig. 2.1

Table 2.1 Resistance change according to the type of MOSs and target gases

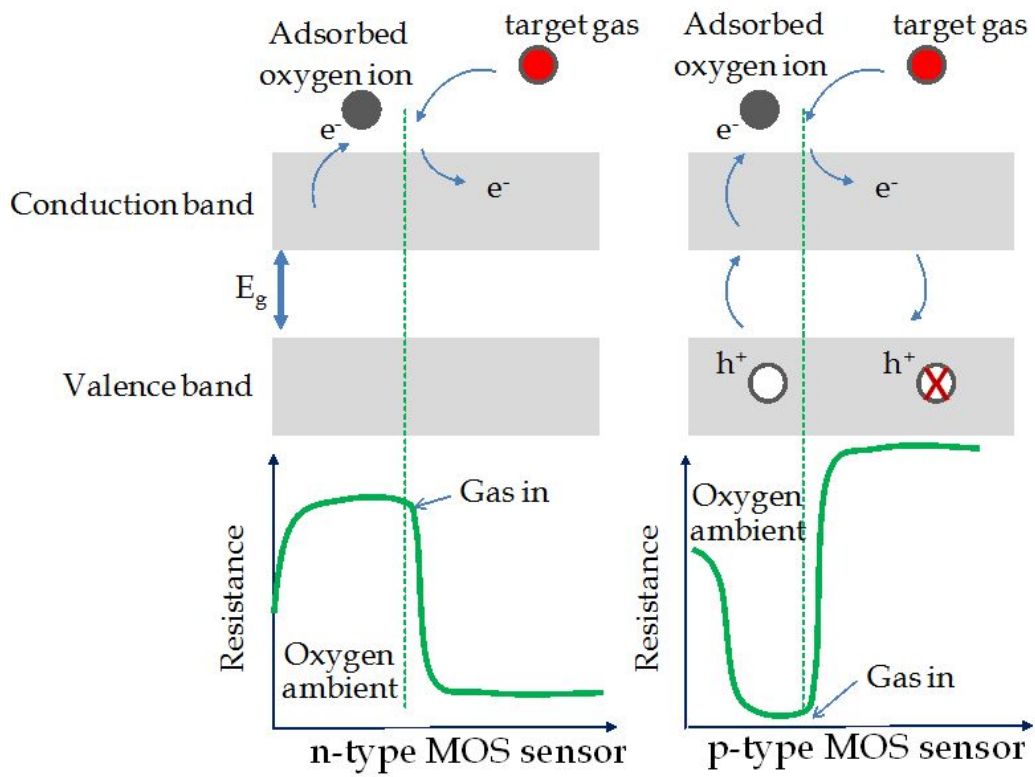| Classification	Oxidizing Gases	Reducing Gases
n-type	Resistance increase	Resistance decrease
p-type	Resistance decrease	Resistance increase

Figure 2.1 Schematic diagram for change of the sensor resistance upon exposure to reducing gas (target gas) in the cases of n-type and p-type semiconductor sensors[16].

2.2 Conduction mechanism in sensing materials

For granular metal oxide sensing materials, the formation of depletion region at the surface of grains and grain boundaries causes the Schottky barriers between the grains. In air, negatively charged oxygen ions are adsorbed to the surface of the sensing materials, as shown in Eq 2.1. In case of n-type semiconductor based gas sensors, the formation of these oxygen adsorbates builds electron depletion region on the surface making a potential barrier at the grain boundaries. When the atmosphere containing reducing gases such as CO approaches to the surface of sensor, the oxygen adsorbates are consumed by subsequent reactions. These reactions lower the potential barrier making electrons to flow easily, thereby decreasing the electrical resistance

During the formation of a depletion layer, the concentration of electrical carrier in volume is decreased in thickness of depletion layer (L_s). Therefore, three conduction mechanisms are possible according to the grain size and *Ls*, as illustrated in Figure 2.2[17]. For large grains (D >> 2L), the conductance of the sensing material is limited by Schottky barriers generated at grain boundaries. In this case, the response (sensitivity) of gas sensors is practically independent of grain size. When grain size is similar to 2L (D = 2L), the resistance in the necks between grains become large enough to influence the total conductivity. In this case, the number of necks determines the conductivity of the sensing material and gas sensitivity. For D > 2L, the case of completely depleted layers, the

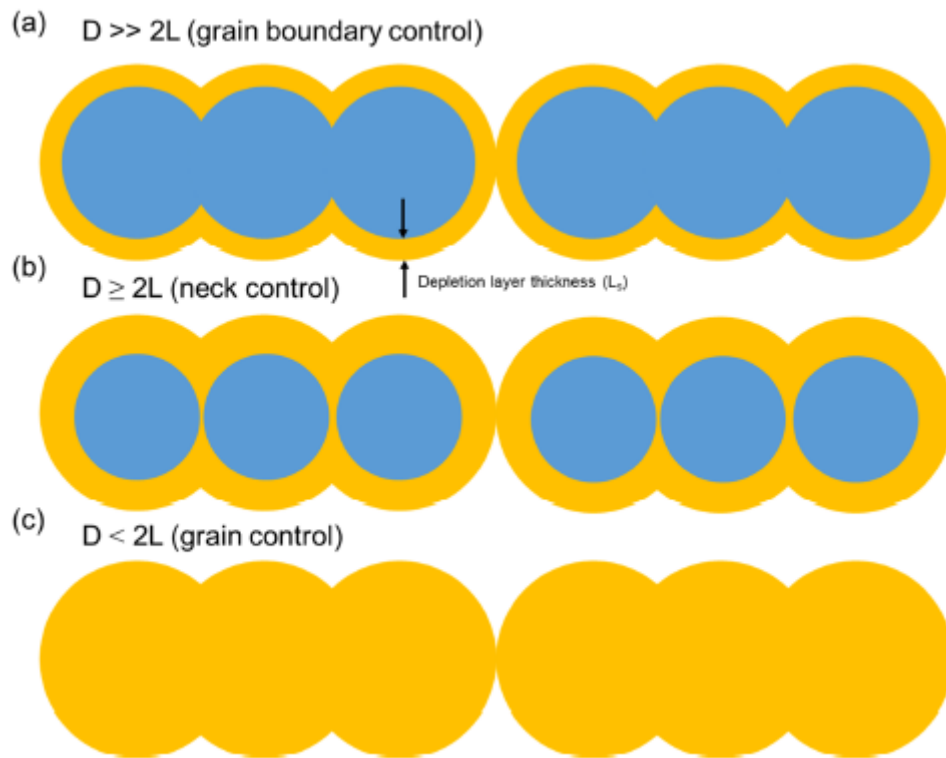conductivity is greatly affected by the charges on the surfaces.

(a) D >> 2L (grain boundary control)

(b) D ≥ 2L (neck control)   Depletion layer thickness (L_s)

(c) D < 2L (grain control)

Figure 2.2 Conduction mechanisms in metal oxide gas sensitive materials according to the grain size. (a) D < 2L, grain boundary control; (b) D = 2L, neck control; (c) D > 2L, grain control.

2.3 Parameters for gas sensor

In order to distinguish the performance of gas sensor, some parameters are used. The most important and essential parameters for gas sensor and their definitions are listed below.

Response and sensitivity

Response of semiconductor gas sensors is defined as the ratio of the measured electrical signal (current, resistance, and voltage) before and after exposing target gas as shown the Eq. 2.4 and 2.5

$$\text{Response} = \frac{R_g}{R_a} \; or \; \frac{R_a}{R_g} \tag{2.4}$$

$$\text{Response (\%)} = \frac{\Delta R}{R_a} \times 100 \; (\%) \tag{2.5}$$

Where R_a is the sensor resistance in ambient air, R_g is the sensor resistance in the target gas, and $\Delta R = |R_a - R_g|$.

Sensitivity (S) of gas sensor is a change of measured signal (for example, response) per analyte concentration; it can be represented by slope of a calibration graph. This parameter is sometimes confused with the limit of detection.

Response time and recovery time

Response time is the time it takes for sensor to changing resistance from 10% to 90% of the equilibrium value upon exposure to target gas. Recovery time is the time required for returning the sensor signal to 90% of its initial value upon removal of the target gas.

Detection limit (DL)

Detection limit is lower limit of detection of the target gas that can be detected by the gas sensor. DL is estimated via extrapolating of sensitivity versus concentration curve and using the Eq. 2.6

$$\text{DL} = \frac{3 \times RMS}{slope} \tag{2.6}$$

Where RMS is root-mean-square deviations[18].

Chapter 3.

Experimental description

3.1 Sensor Fabrication

150-nm-thick Pt films were deposited on SiO_2/Si substrate using an electron beam evaporator. Prior to the Pt deposition, 50-nm-thick Ti was deposited to improve the adhesion of Pt to the SiO_2/Si substrate. Pt IDEs of 5μm spacing were fabricated using photolithography and dry etching. After patterning the Pt IDEs, $α-Fe_2O_3$ (hematite) films were synthesized onto the predefined regions where is uncovered by a ketone tape using hydrothermal method. This hydrothermal procedures were adapted from a previous report and slightly modified[19]. The solution used for hydrothermal was consisting of 0.15M iron (III) chloride, 0.15M urea in 40mL D.I. water. The fabrication occurs at $100^{o}C$, 1~4h in stain-less steel autoclave. These samples are named S1, S2, S3 and S4. After synthesizing, the sample were carefully washed several times with distilled water and dried in nitrogen. The fabricated samples were annealed at $600^{o}C$ for 24h in air ambient to induce from precursor, $β-FeOOH$ to hematite phase transition.

3.2 Characterization

The morphologies of the synthesized nanorods were characterized by Field Emission Scanning Electron Microscope (FE-SEM, Merlin compact) using the acceleration voltage 1kV. The crystallinity and phase of nanorods were characterized by X-Ray Diffraction (XRD, D8 advance). Transmission electron

microscopy (TEM) was performed using a JEM-2100F field emission transmission electron microscope (JEOL, JEM-2100F.). For the TEM analysis, the specimen was prepared by scraping with knife and solving in ethanol.

3.3 Sensor Measurements

The gas sensing properties of the synthesized hematite nanorods sensor were measured in tube furnace by monitoring the change of sensor resistance on changing the Gas sensing properties of the samples were measured in a quartz tube with external heating by a tube furnace. As the flow gas was changed from dry air to a calibrated target gas (balanced with dry air, Sinjin Gases), the variation in the baseline resistance was monitored using a source measurement unit. A constant flow rate of 1000 standard cubic centimeters per minute (sccm) was used for dry air and the target gas. The baseline resistance was measured at a DC bias voltage of 1V using a source measurement unit (Keithley 236). The response of the sensors was accurately determined by measuring the baseline resistance in dry air and the fully saturated resistance after exposure to the target gas. The gas flow was controlled using mass flow controllers and all measurements were recorded on a computer using LabVIEW over the GPIB interface.

Chapter 4.

Results and Discussion

After synthesis, the area of sensing film on Pt IDEs is yellow, as shown in Fig. 4.1(a). In general, material synthesized by our experimental method is known as β-FeOOH []. The yellow film was converted into reddish film after annealing, in Fig. 1(b). β-FeOOH usually turn into α-Fe$_2$O$_3$, hematite by annealing over 500°C for a few hours []. Hematite has been known as reddish color due to its band gap, 2.2eV. There is an obvious contrast of colors between films on Pt electrode and SiO$_2$/Si substrate, in Fig. 4.1(a) and (b), due to the difference of optical interference and nanostructure by bottom films.

Furthermore, in order to reveal the assistance of ketone tape and Pt electrode during α-Fe$_2$O$_3$ synthesis progress, Fig. 4.1(c) and (d) are the photographs of the α-Fe$_2$O$_3$ without Pt electrode on SiO2/Si substrate. It is shown that α-Fe$_2$O$_3$, the reddish film on SiO$_2$, is not uniformly synthesized. That is, Pt electrode helps the formation of α-Fe$_2$O$_3$ film evenly by assisting nucleation. Also, comparing Fig. 4.1(c) and (d), hematite close by ketone tape at Fig. 4.1(d) shows rich dark red, means synthesized much thicker.
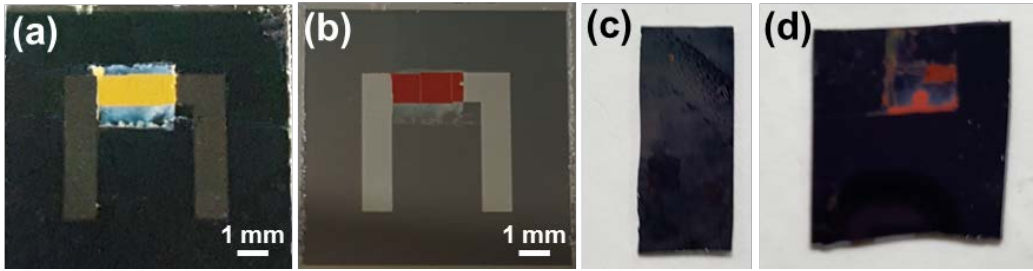
Figure 4.1 Photographs of a fabricated SiO$_2$/Si substrate (a) before annealing, (b) after annealing, and photographs of bare SiO$_2$/Si substrate synthesized (c) with ketone tape, (d) without tape.

The SEM image in Fig. 4.2(a) shows the plain-view of synthesized material on Pt-IDE-patterned SiO_2/Si substrate. The active area between Pt finger electrodes is closely packed with nanorods which has porous and many holes at surface. The high-magnification SEM image in Fig. 4.2(b) shows surface morphology of hematite nanorods. Angled nanorods on Pt electrode are relatively dense compared with those between Pt electrodes. Also, the nanorods on Pt electrode are more vertically aligned and some nanorods between Pt electrodes are inclined very much, since hematite starts nucleation on Pt bottom electrode. The morphology of Pt electrodes and hematite nanorods was clarified by cross-sectional SEM image in Fig. 4.2(c). The red part with flat bottom surface is nanorods on SiO_2/Si substrate, sensing area between Pt electrodes, and yellow part is nanorods on Pt electrode. This result indicates that vertically ordered hematite nanorods could be directly synthesized on Pt-IDE-patterned SiO_2/Si substrate using simple hydrothermal method. To the best of our knowledge, there is no previous study about direct synthesis of hematite nanorod array on a SiO_2/Si substrate.
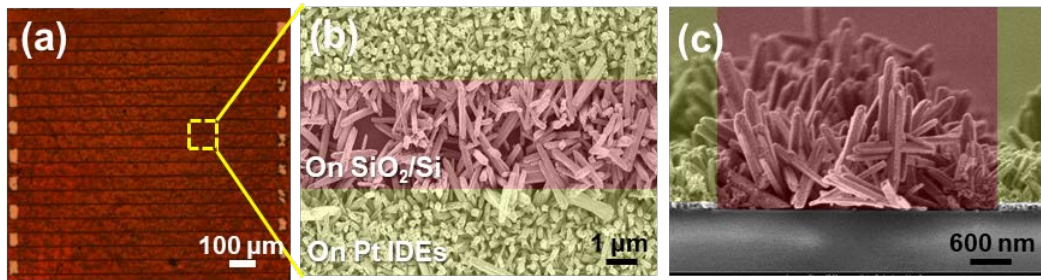
Figure 4.2 (a) Optical microscope image of hematite nanorods array on Pt IDE patterned SiO2/Si substrate. (b) High-magnification SEM image of selected area in (a). (c) cross-sectional SEM image of hematite nanorods array.

The SEM images in Fig. 4.3 show morphology change of hematite nanorods on Pt-IDE-patterned SiO_2/Si substrate by synthesis time. S1, in Fig. 4.3(a) and (e), stopped the growth before completing the formation of nanorod shape. These grain-like nanorods cover the entire substrate, but SiO_2 between Pt finger electrodes remains empty space. As there is not much length difference between hematite nanorods on Pt electrode and SiO_2 substrate, the nucleation occurs more frequently on Pt electrode than SiO_2 substrate during synthesis. The nanorods on S1 have porous structure with many holes on the surface. In Fig. 4.3(b) and (f), S2 is formed rod shape hematite completely. The surface of nanorods is same as S1, porous and punctured. Also, angled nanorods on Pt electrode are relatively dense compared with those between Pt electrodes. That is, nucleation mainly occurs on Pt electrode, which helps the growth of nanorods on SiO_2 substrate. However, nanorods between Pt electrodes are longer than those on Pt electrode. S3 shows more dense nanorods film between Pt electrodes, in Fig. 4.3(c). In Fig. 4.3(g), nanorods are aggregated like porous film at the bottom side of dense nanorods. During synthesis, repetitive dissolution and precipitation which occur in aqueous precursor solution change nanostructure from complete nanorod shape to aggregated porous film. S4 in Fig 4.3(d) and (h), has nanorods thicker than S3, however, the length is not much different. Also, the bottom side of nanorods is aggregated like S3.
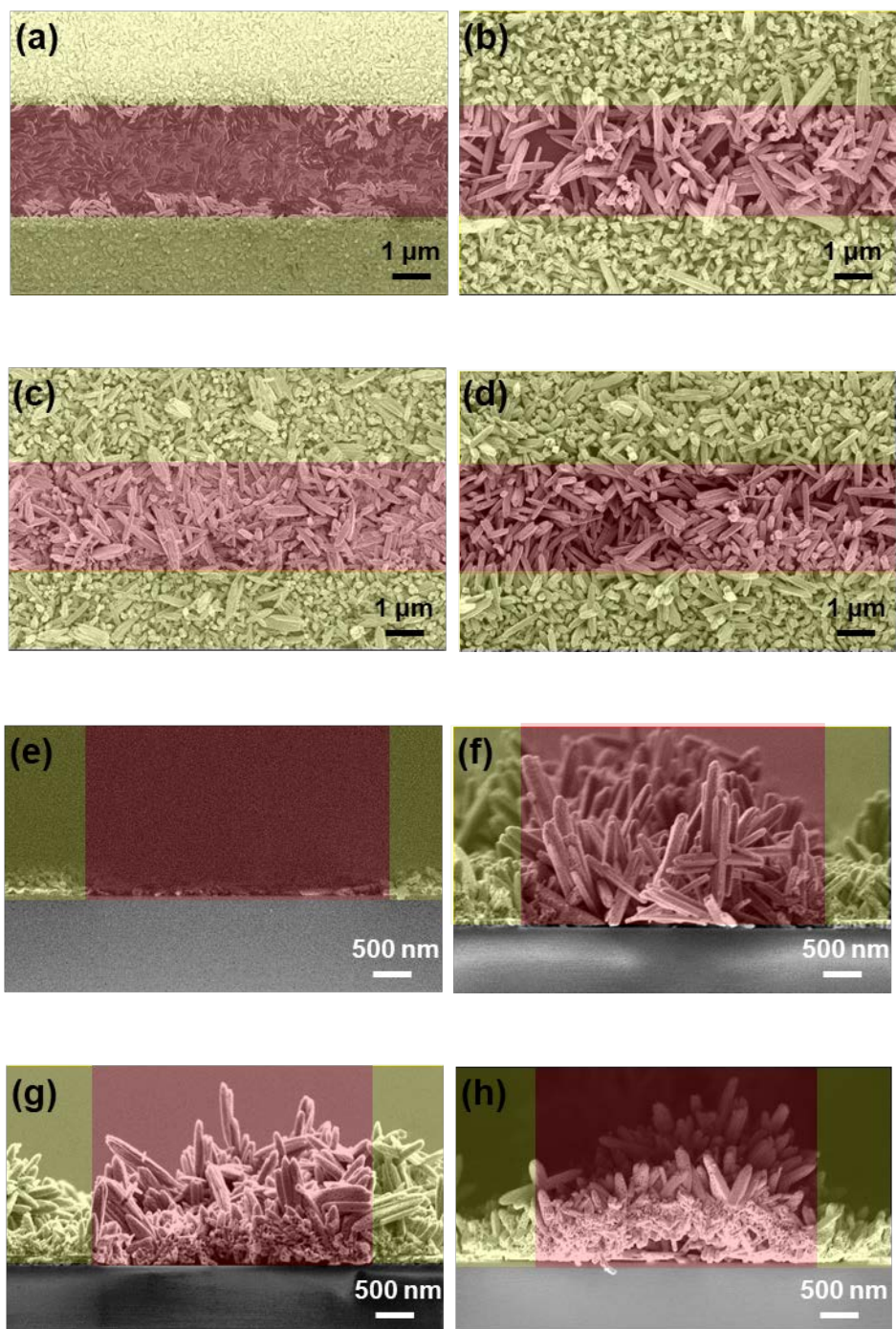
Figure 4.3 (a-d) Plain-view SEM image of (a) S1, (b) S2, (c) S3, (d) S4 and (e-h) cross-sectional SEM image of (e) S1, (f) S2, (g) S3, (h) S4

The crystal structure and crystallinity of hematite nanorods were characterized by TEM and XRD measurement. The TEM image in Fig. 4.4(a) shows a single scraped nanorods. It indicates that the diameter of rod is ~90nm. The rod in TEM image is variegated, this is because the rod does not have a tidy surface with many cavities. However, the high-resolution TEM image in Fig. 2(b) reveals that hematite nanorods have high crystallinity. The selected area electron diffraction pattern in inset of Fig. 4.4(b) also proves that high crystalline property of hematite nanorods synthesized by hydrothermal method. These nanorods are faceted with a (-102) and (0-11) plane with interplanar spacing of 3.683Å and 4.157Å.
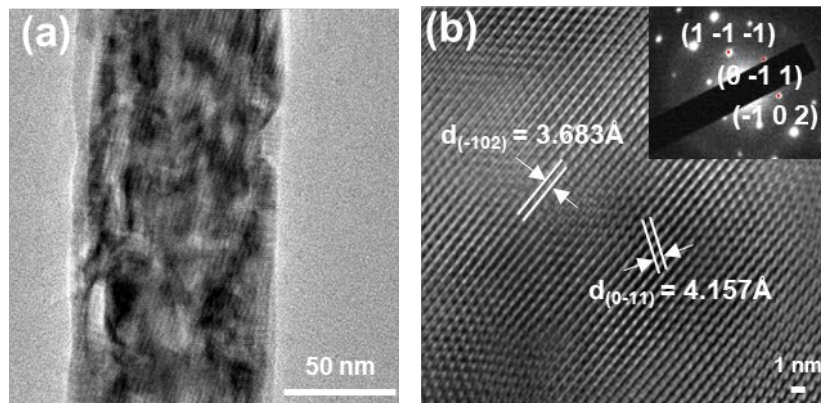
Figure 4.4 (a) Low-magnification TEM image of scraped hematite nanorod. (b) High-magnification TEM image of hematite nanorod. The inset shows selected area diffraction pattern with indexing.

The XRD pattern of hematite nanorods is presented on Fig 4.5. The peak positions correspond to the reflection of the hexagonal phase of hematite (JCPDS #33-0664). Regardless of synthesis time, all samples show similar diffraction patterns. The hematite nanorods has (104) as main peak. It is considered that (104) has the highest surface energy, this should be revealed in follow studies. No β–FeOOH peak is observed from annealed samples, which confirms the complete transition of β–FeOOH to α-Fe_2O_3. Also, these patterns show sharp peaks on same position corresponding to the hematite phase without second phases.
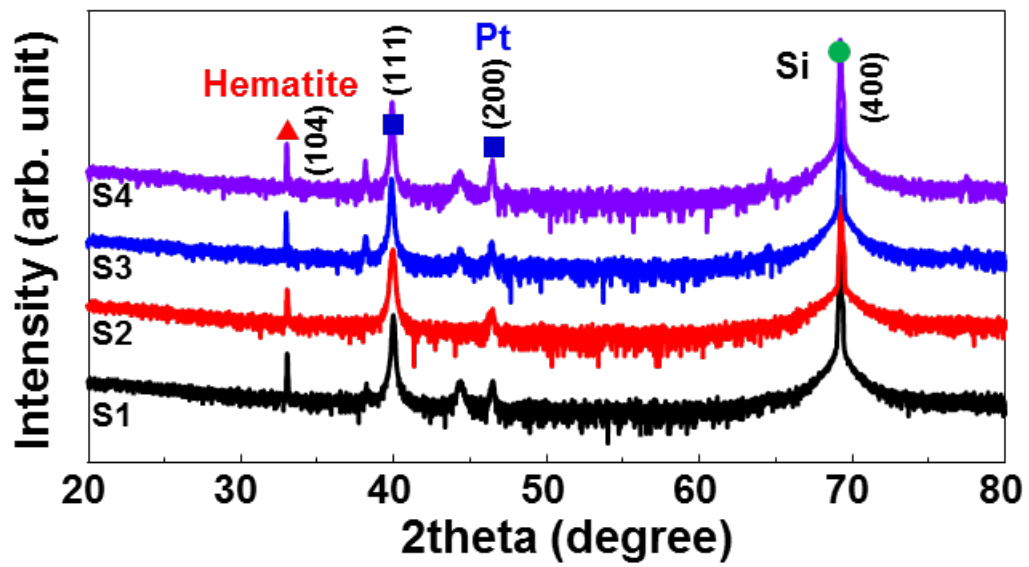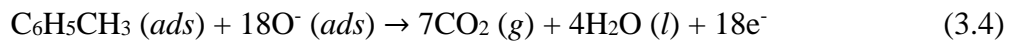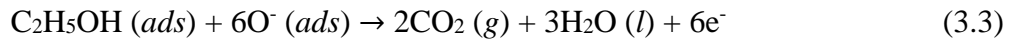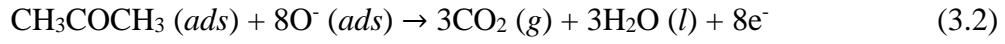
Figure 4.5 Glancing angle X-ray diffraction patterns of hematite nanorods array S1~S4.

First, in order to find the best synthesis time for gas sensing, responses to VOCs are measured. The response curve of hematite nanorods to 50ppm acetone, ethanol, and toluene was indicated in Fig. 4.6. The response, S, is defined as (R_{air} - R_{gas})/R_{gas} for the reducing gases (acetone, ethanol, toluene, CO, H_2, C_6H_6, C_7H_8, NH_3, and CH_3CHO) where R_{air} and R_{gas} denote resistances in air and tested gas atmosphere, respectively. When hematite nanorods were exposure to target gases, the resistance of hematite nanorods was decreased as typical n-type semiconductor metal oxide. Compared to the response of other samples, S2 has the highest response among S1~4. Especially, the response to ethanol of S2 is larger than 3 times the response of other samples. However, in other samples, response to ethanol does not show that much difference. The resistance of S4 was more decreased when S4 was exposure to acetone. The gas sensing mechanism of the hematite nanorods can be explained by the surface-depletion model[20]. When the hematite nanorods are exposed to dry air, oxygen ions are adsorbed onto the surface. Therefore, the depletion layer extends to deeper region of the hematite nanorods, which leads to high resistance. On the other hands, upon exposure to reducing gas such as acetone, ethanol and toluene, chemisorbed oxygen ions at the surface of hematite nanorods are reacted with target gas molecules to form CO_2 and H_2O:

$$O^2 \ (g) + 2e^- \rightarrow 2O^- \ (ads) \tag{3.1}$$

$$CH_3COCH_3 \ (ads) + 8O^- \ (ads) \rightarrow 3CO_2 \ (g) + 3H_2O \ (l) + 8e^- \qquad (3.2)$$

$$C_2H_5OH \ (ads) + 6O^- \ (ads) \rightarrow 2CO_2 \ (g) + 3H_2O \ (l) + 6e^- \qquad (3.3)$$

$$C_6H_5CH_3 \ (ads) + 18O^- \ (ads) \rightarrow 7CO_2 \ (g) + 4H_2O \ (l) + 18e^- \qquad (3.4)$$

This reaction generates charge carrier in the hematite nanorods and narrow the depletion layer width at the surface, which causes decrease of the resistance of hematite nanorods:
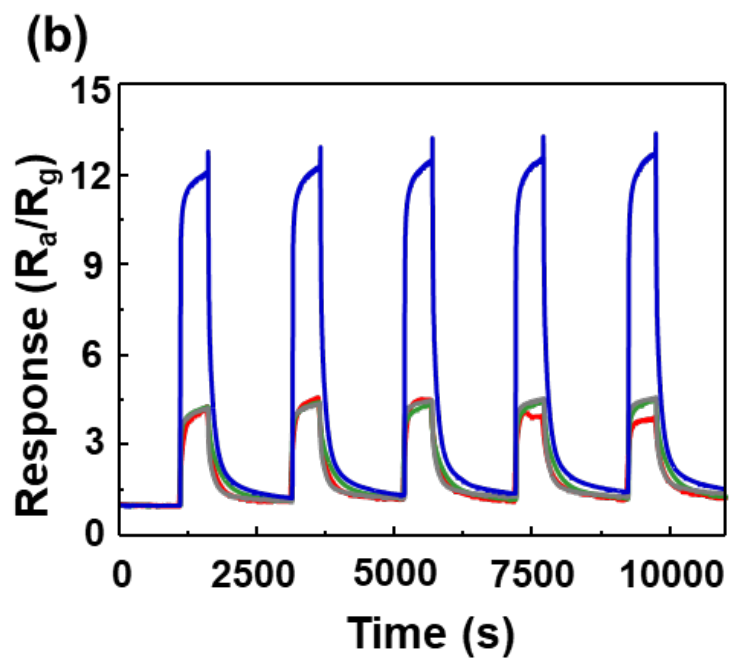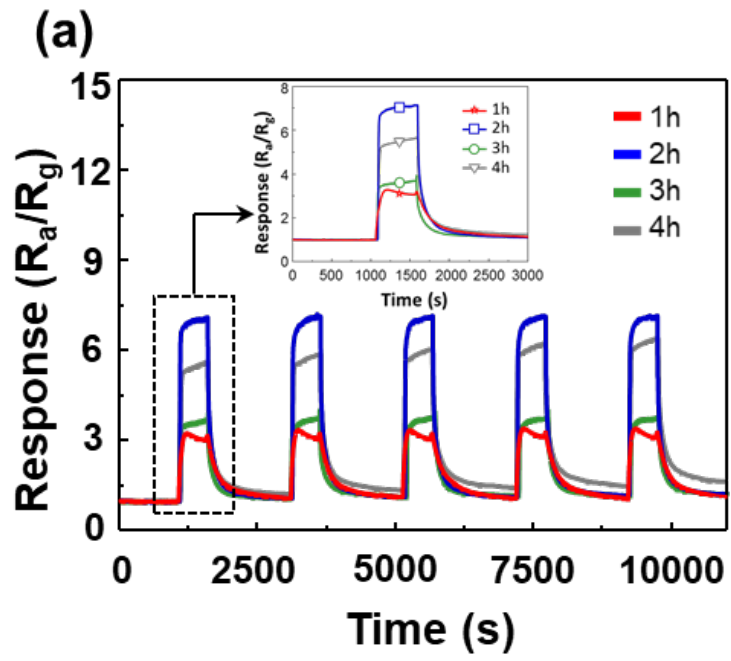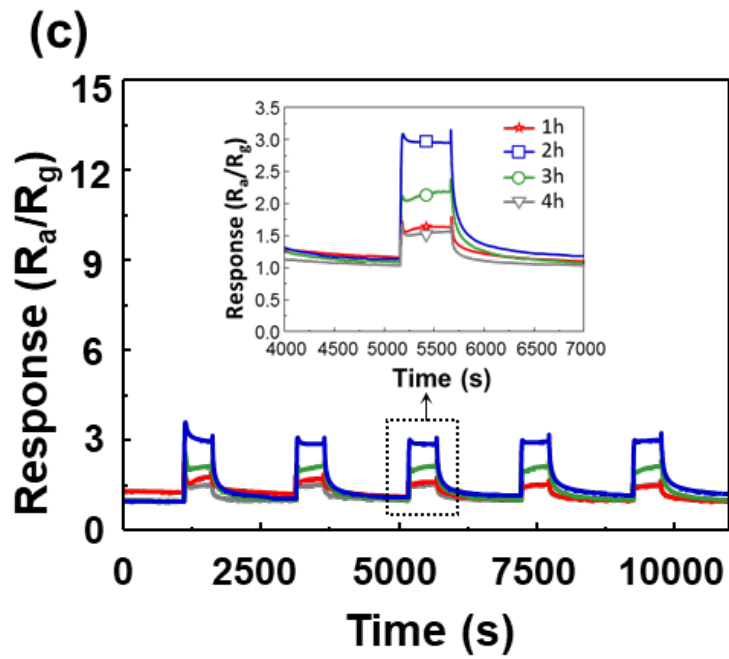
Figure 4.6 Response curves of S1, S2, S3, S4 to 50ppm (a) acetone, (b) ethanol, and (c) toluene. Red, blue, green and gray curves are response of S1, S2, S3, and S4, respectively.

Operating temperature, which changes base resistance and response of sensor, is one of the important factors for gas sensors. To find the optimum operating temperature for best response, we measured the responses to 50ppm acetone, ethanol, toluene at 300~400°C of S2 in Fig. 4.7(a). The hematite nanorods show the best response to ethanol at 350°C. The response ratio, $S_{ethanol}/S_{acetone}$, is higher than 1.7. Not only extremely high sensitivity, the hematite nanorods also exhibits supreme selectivity to ethanol at the temperature. S2 indicates relatively low response to acetone at 350°C and the response of S2 to acetone increased continuously until 400°C. Besides, Optimum operating temperature to acetone could be higher temperature. Under toluene atmosphere, S2 shows similar response curve shape with response curve to ethanol, however, the response value is generally much lower than response values to acetone and ethanol. Therefore, it clearly shows that optimum operating temperature to each gases is different. The response of S1 ~ 4 to 50ppm acetone, ethanol, toluene at 350°C is shown in Fig. 4.7(b). Compared with SEM images in Fig. 4.3, S1 which stopped at nucleation phase indicated very low responses to all 3 gases. The highest response was shown in S2 due to vertically grown nanorods. Vertically aligned nanorods maximize the surface-to-volume ratio. This would be explained more in later part. On the contrary to this, collapsed nanorods led sharply declined surface-to-volume ratio and response in S3. Similarly, S4 shows overlapped nanorods which caused low surface area and responses.
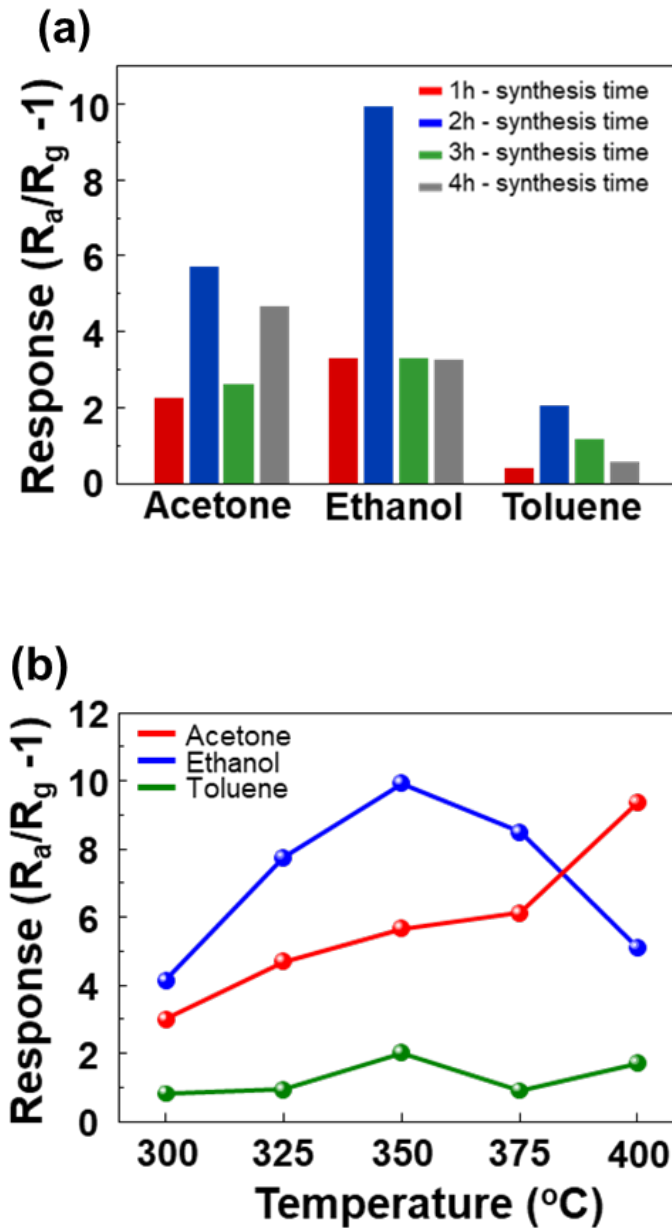
Figure 4.7 (a) Response of S2 to 50ppm acetone, ethanol and toluene as a function of temperature. (b) Response of S1~S4 at 350oC to 50 ppm acetone, ethanol, and toluene.

Additionally, to identify the selectivity of hematite nanorods to VOCs, we measured the response to various gases in 50 ppm such as CO, C_6H_6, NH_3, H_2, and CH_3CHO at 350°C and arrange them to typical response graph and bar graph in Fig. 4.8(a) and (b). We could confirm that the hematite nanorods showed the highest response toward ethanol gas as opposed to any other gases. Response to ethanol is about 2 times higher than response to other gases could demonstrate selectivity of sensing property. To evaluate the detection limits of the hematite nanorods array to ethanol, we measured the response curves of the hematite nanorods array to 10~50 ppm ethanol at 350°C in Fig. 4.9(a). The responses of the hematite nanorods array were 6.85, 8.80, 10.34, 11.48, and 12.44 to 10, 20, 30, 40, and 50 ppm ethanol, respectively. Although the 10 ppm concentration was the lowest experimentally examined in the present study, the theoretical detection limit (signal-to-noise ratio >3)[18] is calculated to be approximately 21.05 ppb. The detection limits of ppb levels to ethanol show the possibility of the sensors to highly sensitive ethanol sensors. Fig. 4.9(b) shows response to consecutive pulses of 10~50 ppm ethanol.
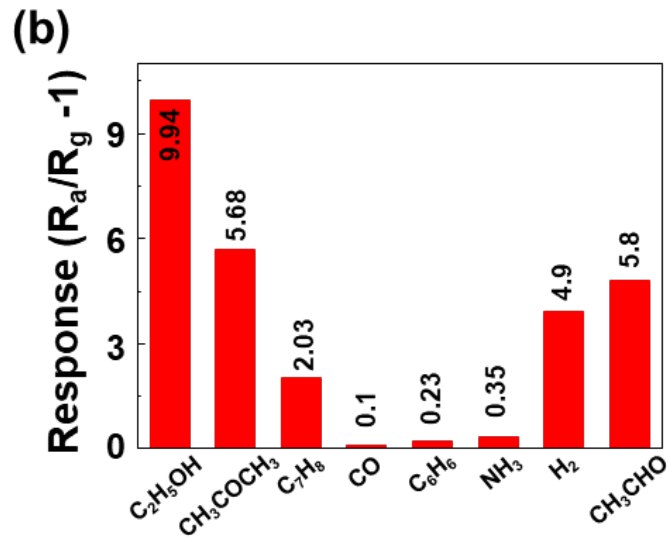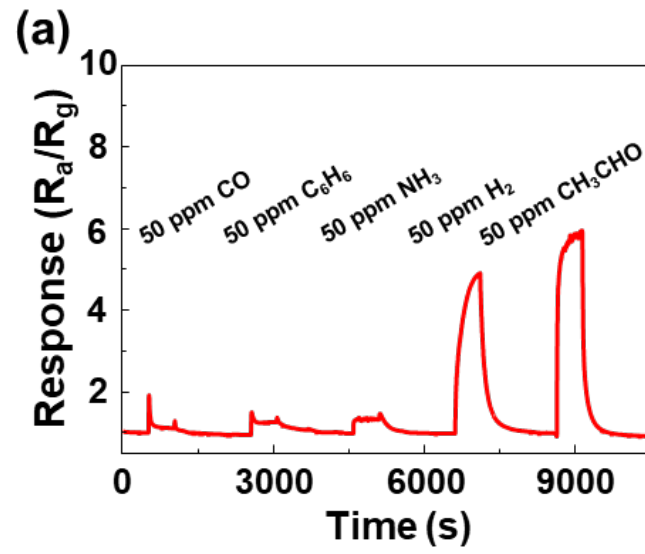
Figure 4.8 (a) Sensing transient of S2 to various gases. (b) Response of S2 to various gases.
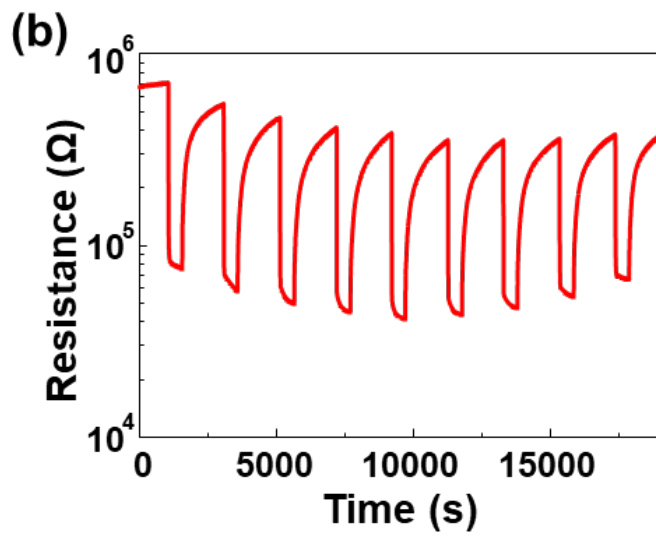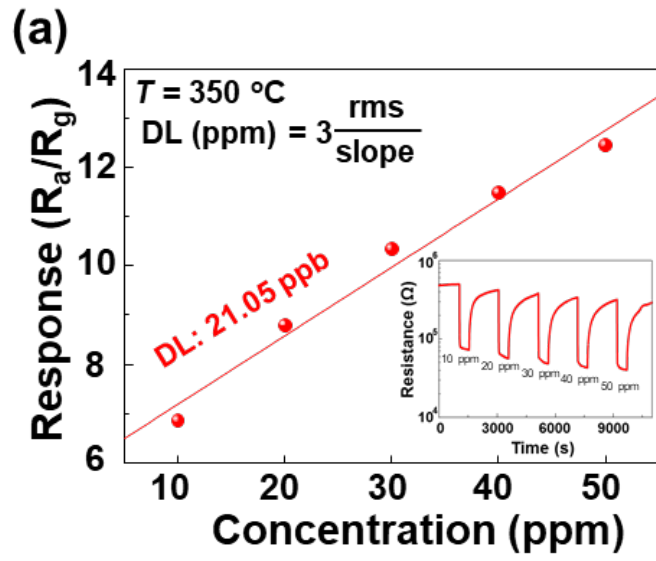
Figure 4.9 (a) Theoretical detection limits (DL) of S2 to ethanol. Inset shows response curve to 10-50 ppm ethanol at 350°C. (b) Response to 9 consecutive pulse of S2 to 10-50 ppm ethanol.

Fig. 4.10 is a schematic diagram of nanostructure. It is well known that gas sensing performance of semiconductor is controlled by three major factors, receptor function, transducer function, and utility factor [1]. Fig 4.10(a) shows the simple drawing of S2. Such a rod-only structure is able to accept target gas molecules up to the bottom side. The gas molecules attached to the surface of nanorods from the top to the bottom change the current path by modifying depletion region wider or narrower. However, when the porous nanorods are aggregated at the bottom side, gas molecules are only attached to topside of porous nanorods. Since current flows through porous rods as drawn in the Fig. 4.10(b), depletion region produced at topside only cannot affects total resistance much. Therefore, sensors with nanostructure that porous nanorods are aggregated below the nanorods like S3 have considerably low response to target gases.
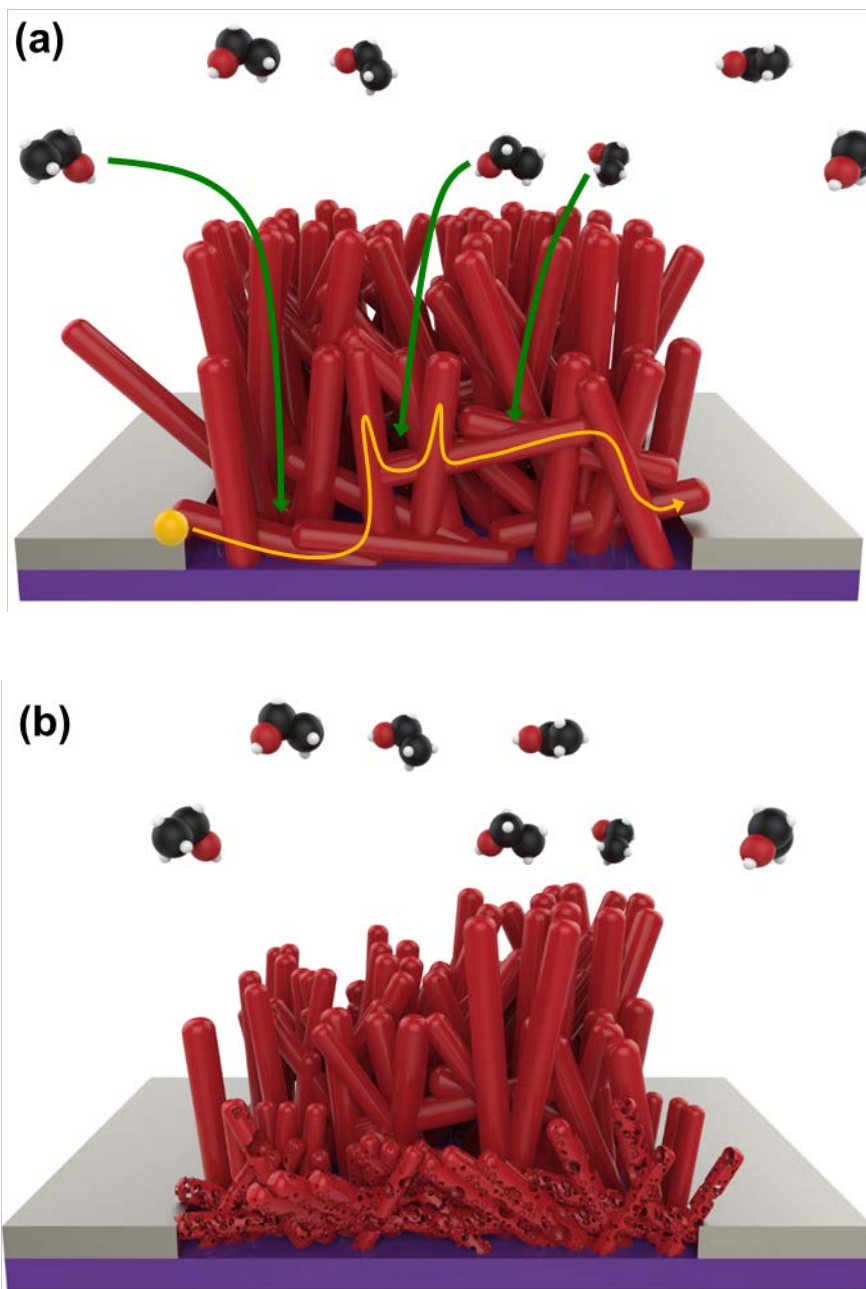
Figure 4.10 Schematic drawing of hematite nanostructure (a) with complete rods (b) with porous rods. Molecules at top side are sphere model of ethanol and yellow sphere is electron. Green line is gas acceptance way and yellow line is current path.

Chapter 5.

Conclusion

In summary, we have developed a facile and viable hydrothermal method to obtain vertically aligned hematite nanorod array for sensor application. Using hydrothermal method, hematite nanorods could be directly synthesized on patterned SiO_2/Si substrate and applied for gas sensors without additional process. The responses of S2 to various gases such as ethanol, acetone, CO, C_6H_6, NH_3, H_2, and CH_3CHO were much higher than those of other samples. Especially, our hematite nanorods displayed high and selective response to ethanol with theoretical detection limits down to a few parts per billion. Excellent selectivity and ppb level detection limits to ethanol show the potential of hematite nanorods for breath analysers to detect alcohol. These results were attributed to the vertically standing nanostructures which enhance the utility factors much better. The facileness of fabrication and large-scale productivity hold the promise for future applications including photoelectrochemical cell and batteries where 1-D nanostructure plays a role due to high surface-to-volume ratio.

References

[1] N. Yamazoe, Toward innovations of gas sensor technology, Sens. Actuators B 187 (2013) 162–167

[2] Y.S. Shim, D.H. Kim, H.Y. Jeong, Y.H. Kim, S.H. Nahm, C.Y. Kang, J.S. Kim, W. Lee, H.W. Jang, Utilization of both-side metal decoration in close-packed SnO_2 nanodome arrays for ultrasensitive gas sensing, Sens. Actuators B 213 (2015) 314-321

[3] Y.H. Kim, K.Y. Kim, Y.R. Choi, Y.S. Shim, J.M. Jeon, J.H. Lee, S.Y. Kim, S. Han, H.W. Jang, Ultrasensitive Reversible Oxygen Sensing in Liquid-Exfoliated MoS_2 Nanoparticles, J. Mater. Chem. A 4 (2016) 6070-6076

[4] P. Sun, Z. Zhu, P. Zhao, X. Liang, Y. Sun, F. Liu, G. Lu, Gas sensing with hollow α-Fe_2O_3 urchin-like spheres prepared via template-free hydrothermal synthesis, CrystEngComm 14 (2012), 8335-8337

[5] Z. Wu, K. Yu, S. Zhang, Y. Xie, Hematite Hollow Spheres with a Mesoporous Shell: Controlled Synthesis and Applications in Gas Sensor and Lithium Ion Batteries, J. Phys. Chem. C 112 (2008), 11307-11313

[6] H.J. Kim, K.I. Choi, A. Pan, I.D. Kim, H.R. Kim, K.M. Kim, C.W. Na, C. Cao, J.H. Lee, Template-free solvothermal synthesis of hollow hematite spheres and their applications in gas sensors and Li-ion batteries, J. Mater. Chem. 21 (2011) 6549-6555

[7] D.H. Kim, Y.S. Shim, H.G. Moon, H.J. Chang, D. Su, S.Y. Kim, J.S. Kim, B.K. Ju, S.J. Yoon, H.W. Jang, Highly Ordered TiO_2 Nanotubes on Patterned Substrates: Synthesis-in-Place for Ultrasensitive Chemiresistors, J. Phys. Chem. C. 117 (2013) 17824-17831

[8] Y.S. Shim, H.G. Moon, D.H. Kim, L. Zhang, S.J. Yoon, Y.S. Yoon, C.Y. Kang, H.W. Jang, Au-decorated WO_3 cross-linked nanodomes for ultrahigh sensitive and selective sensing of NO_2 and C_2H_5OH, RSC Advances 3 (2013) 10452

[9] K. Aguir, C. Lemire, D.B.B. Lollman, Electrical properties of reactively sputtered WO_3 thin films as ozone gas sensor, Sens. Actuators B 84 (2002) 1-5

[10] N. Barsan, D. Koziej, U. Weimar, Metal oxide-based gas sensor research: how to?, Sens. Actuators B 121 (2007) 18-35.

[11] J.M. Jeon, Y.S. Shim, S.D. Han, D.H. Kim, Y.H. Kim, C.Y. Kang, J.S. Kim, M. Kim, H.W. Jang, Vertically ordered SnO_2 nanobamboos for substantially improved detection of volatile reducing gases, J. Mater. Chem. A 3 (2015) 17939-17945

[12] D.H. Kim, Y.S. Shim, J.M. Jeon, H.Y. Jeong, S.S. Park, Y.W. Kim, J.S. Kim, J.H. Lee, H.W. Jang, Vertically Ordered Hematite Nanotube Array as an Ultrasensitive and Rapid Response Aceton Sensor, ACS Appl. Mater. & Interfaces 6 (2014) 14779-14784

[13] X.L. Fang, C. Chen, M.S. Jin, Q. Kuang, Z.X. Xie, S.Y. Xie, R.B. Huang,

L.S. Zheng, Single-crystal-like hematite colloidal nanocrystal clusters: synthesis and applications in gas sensors, photocatalysis and water treatment, J. Mater. Chem 19 (2009) 6154-6160

 [14] C. Wu, P. Yin, X. Zhu, C.O, Y. Xie, Synthesis of Hematite (α-Fe2O3) Nanorods: Diameter-Size and Shape Effects on Their Applications in Magnetism, Lithium Ion Battery, and Gas Sensors, J. Phys. Chem. B 110 (2006) 17806-17812

[15] X. Hu, J.C. Yu, J. Gong, Q. Li, G. Li, α-Fe2O3 Nanorings Prepared by a Microwave-Assisted Hydrothermal Process and Their Sensing Properties, Adv. Mater 19 (2007) 2324-2329

[16] S. Choopun, N. Hongsith, E. Wongrat, Metal-oxide nanowires for gas sensors (X. Peng, Ed.), Intech (2012)

[17] V.E. Bochenkov and G. B. Sergeev, Sensitivity, selectivity, and stability of gas-sensitive metal-oxide nanostructures (A. Umar and Y.-B. Hahn. Ed.), 3, (2010) 34-52

[18] J. Li, Y. Lu, Q. Ye, M. Cinke, J. Han, M. Meyyappan, Carbon Nanotube Sensors for Gas and Organic Vapor Detection, Nano Lett. 3 (2003) 929-933

[19] Gurudayal, S.Y. Chiam, M.H. Kumar, P.S. Bassi, H.L. Seng, J. Barber, L.H. Wong, Improving the Efficiency of Hematite Nanorods for Photoelectrochemical Water Splitting by Doping with Manganese, ACS Appl. Mater. Interfaces 6 (2014) 5852-5859

[20] P. Feng, Q. Wan, T.H. Wang, Contact-controlled sensing properties of flowerlike ZnO nanostructures, Appl. Phys. Lett. 87 (2005) 213111

초 록

IDE와 같은 패턴이 새겨져 있는 기판에 고 결정성 산화철 나노막대를 통합하는 것은 높은 부피 대비 표면적 비와 장기간 안정성과 같은 1차원 나노막대 구조의 장점을 취할 수 있는 효과적인 디자인 계획이지만, 합성 과정에서 많은 부분이 도전과제로 남아있다. 우리는 추가 과정이 없는 간단한 산화철 나노막대 박막의 합성 방법과 이 박막의 가스 센서로의 활용을 발표한다.

수직으로 서 있는 산화철 나노막대는 수열합성법으로 합성되었다. 산화철 나노막대의 형태는 합성 시간을 바꾸면서 조절되었다. 수직으로 서 있는 산화철 나노막대의 350도에서 50ppm의 에탄올에 대한 반응이 무너진 나노막대의 반응보다 4배 더 높았으며, 이론적인 감지 한계는 대략 20ppb로 추측된다. 이는 산화물 층의 바닥부분까지 기체가 확산되는, 소위 유용성 요인으로 설명할 수 있다. 이 센서는 300도에서 375도까지 에탄올에 대해 선택적인 반응을 나타낸다. 우리의 연구 결과는 간단한 합성 방법을 사용하여 형태를 조절하는 것이 지표에 풍부한 반도체 산화물인 산화철에 기반한 에탄올 또는 아세톤 센서를 만드는데 효과적인 전략임을 증명한다.

주요어 : 산화철 나노막대, 수열합성법, 형상 제어, 가스 센서

학번 : 2013-20614